

## PRESENTATION SESSION NO. 2

- PROPULSOR

- CAVITATION

Chairman: Dr. J.B. Hadler

### PS-2.1

**A. HAIMOV, D MINCHEV and R. KALCHEV**  
**Bulgarian Ship Hydrodynamics Centre, Varna,**  
**Bulgaria**

#### **A DEFORMED SLIPSTREAM MODEL USED FOR PROPELLER PERFORMANCE PREDICTION**

##### **1. INTRODUCTION**

Several slipstream models have been used for mathematical presentation of the propeller in the design and performance prediction procedures Ref. [1-5]. Most of them use empirical information for the geometrical parameters of the slipstream to reduce the amount of calculations needed.

The present development is based on a free-slipstream analysis, leading to an iterative procedure for the propeller performance prediction. It appeared from [6] that a similar condition for the design is used in Newcastle.

##### **2. BRIEF OUTLINE OF THE METHOD**

The propeller hydrodynamic model is based on the steady lifting surface theory, characterized by finite circulation at the hub and continuous vorticity and sources distributions for the loading and thickness effects. A curvilinear orthogonal coordinate system on the reference surface and the normal velocity boundary condition yield an integral equation for the bound vorticity strength, the free vorticity being deduced

from the continuity equation using double series presentation. The boundary condition accounts for the three components of induced and inflow velocity. Pressure distribution and forces on the blades are finally calculated by using Bernoulli's and Joukowski's formulae.

The non-linearity of the problem is involved by the boundary condition for the alignment of vortex lines to the flow:

$$\vec{V} \times d\vec{S} = 0 \quad (1)$$

and continuity of vortex tubes:

$$\nabla \cdot \vec{\Omega} = 0 \quad (2)$$

where  $\vec{V}$  - vector of total velocity  
 $d\vec{S}$  - element of the vortex line in the slipstream  
 $\vec{\Omega}$  - vorticity vector

The initial conditions for the velocity field are obtained from the linear approach of regular helicoidal slipstream. The inner iteration loop is for the shape of the deformed stream-vortex lines of the transition wake in the frozen velocity field of current outer iteration satisfying Eq. (1) and (2). The concept of transition wake is similar to that of Kerwin, extending about one propeller radius downstream. The ultimate wake is of constant pitch and strength, those values being obtained by calculations at the points of transition.

For calculation of velocity induced by the lifting surface and the transition wake first order triangular vortex patches are used.

More detailed description of the algorithm is presented in Ref. [7], [8]. It should be noted that the full procedure requests about four hours on a VAX-type computer.

### 3. VALIDATION

First, careful testing of the computer code is performed for the modules of the program package. The choice of the computational mesh for the deformed slipstream program has been made by comparison with the regular helical wake computations.

The sensitivity of the induced velocity to the mesh parameters has been also revealed.

An important point is the convergence of the iterative procedure. Figure 1 shows typical behaviour of the induced velocity, the third inner iteration satisfying the precision criteria. The convergence of the slipstream shape is even more pronounced. However, for very high loadings, in some cases a divergence is observed, due to the high strength of tip vortices and decreasing precision of self-induced velocity calculation.

The impact of the deformed slipstream to the open water prediction for DTRC propeller series [9] is presented in Figure 2.

More detailed validation of the predicted velocity field is performed by using Laser-Doppler Anemometer (LDA) [10]. This is a one-component, three-axis traversing optical system, working in forward scatter dual-beam mode in the cavitation tunnel of BSHC. The three components are measured consequently.

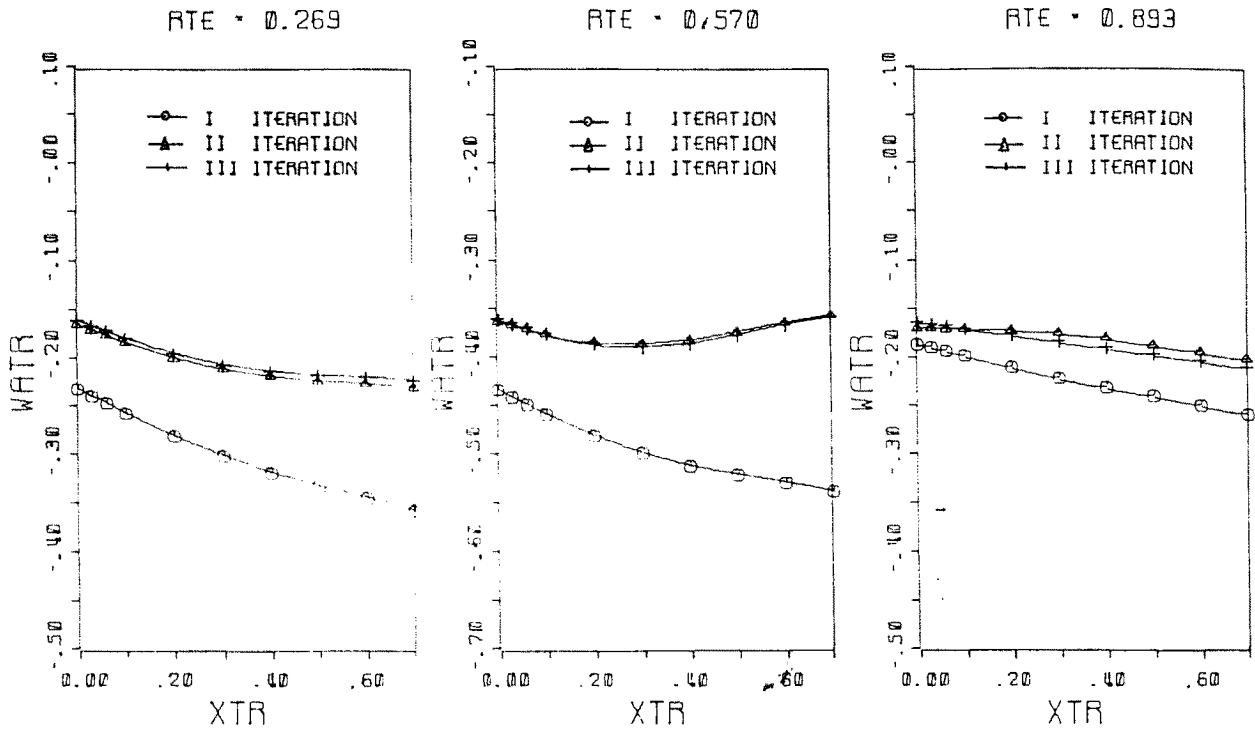


Figure 1 Total axial induced velocity on the vortex sheet of the transition wake.

RTE - relative radius at trailing edge  
 XTR - axial coordinate in the slipstream

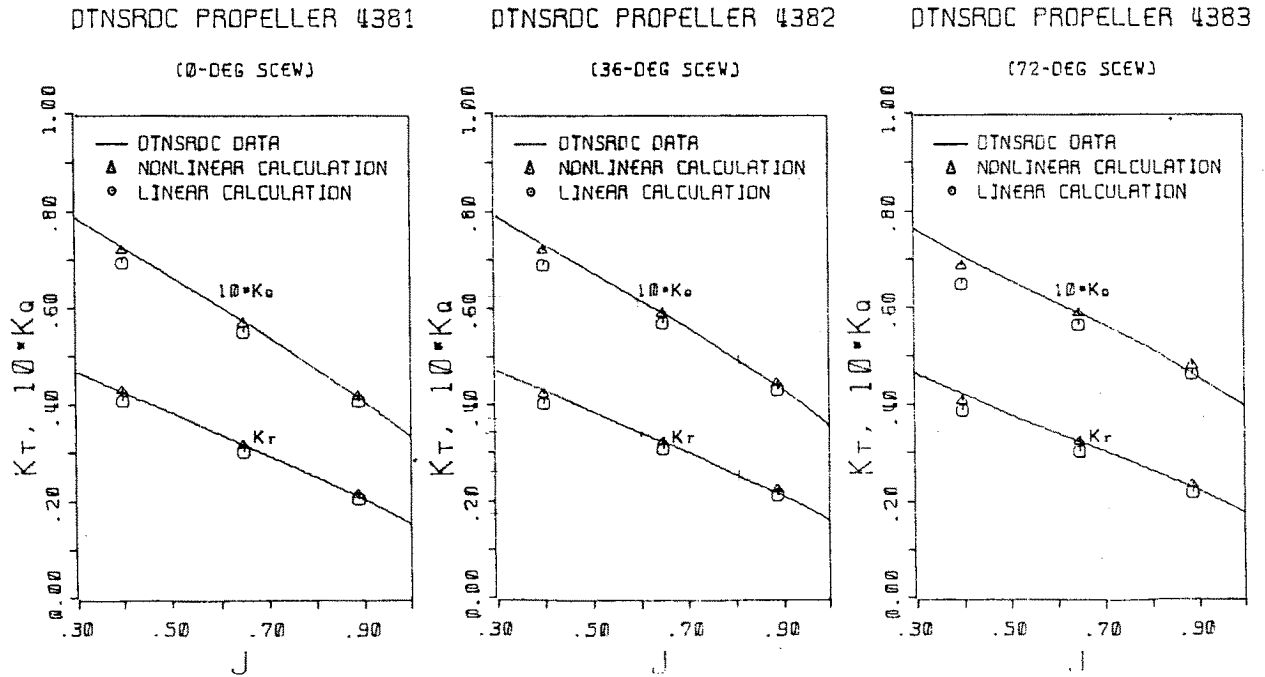


Figure 2 Open water characteristics compared with present predictions.

The computerized data acquisition system accumulates 20,000 valid signals for each scanned location and sorts data points according to propeller blade phase, corresponding to 100 angular positions. Figure 3 shows the mean values of the total axial and tangential velocity, measured and calculated for the HSVA

propeller [11]. In Figure 4 are plotted the circumferential variations of axial and tangential components of velocity at some of the more than 25 radial positions measured. Another way of representing the measuring results and their standard deviations is given in Figure 5.

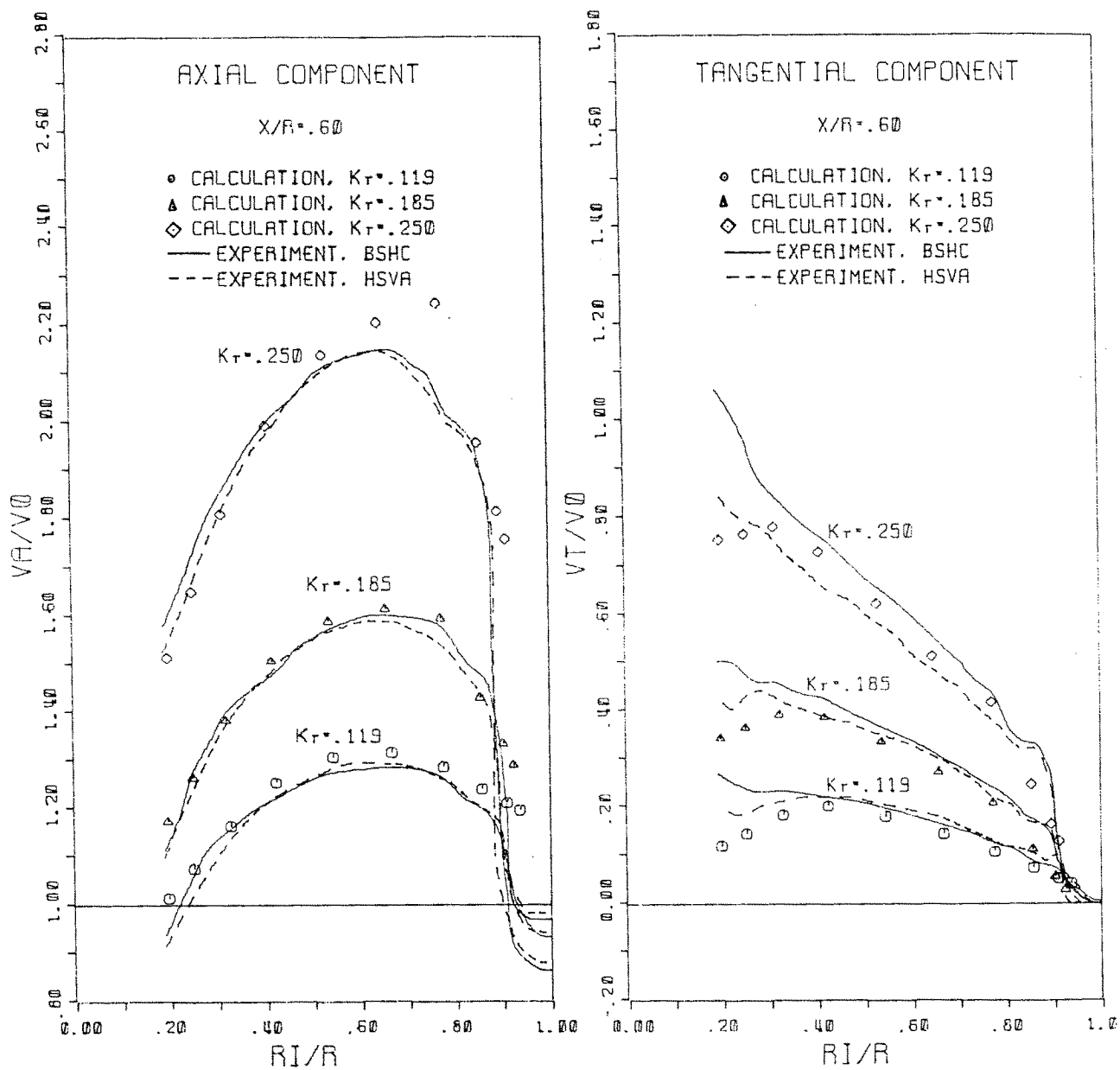


Figure 3 Mean velocity components in the slipstream cross-section for three loadings.

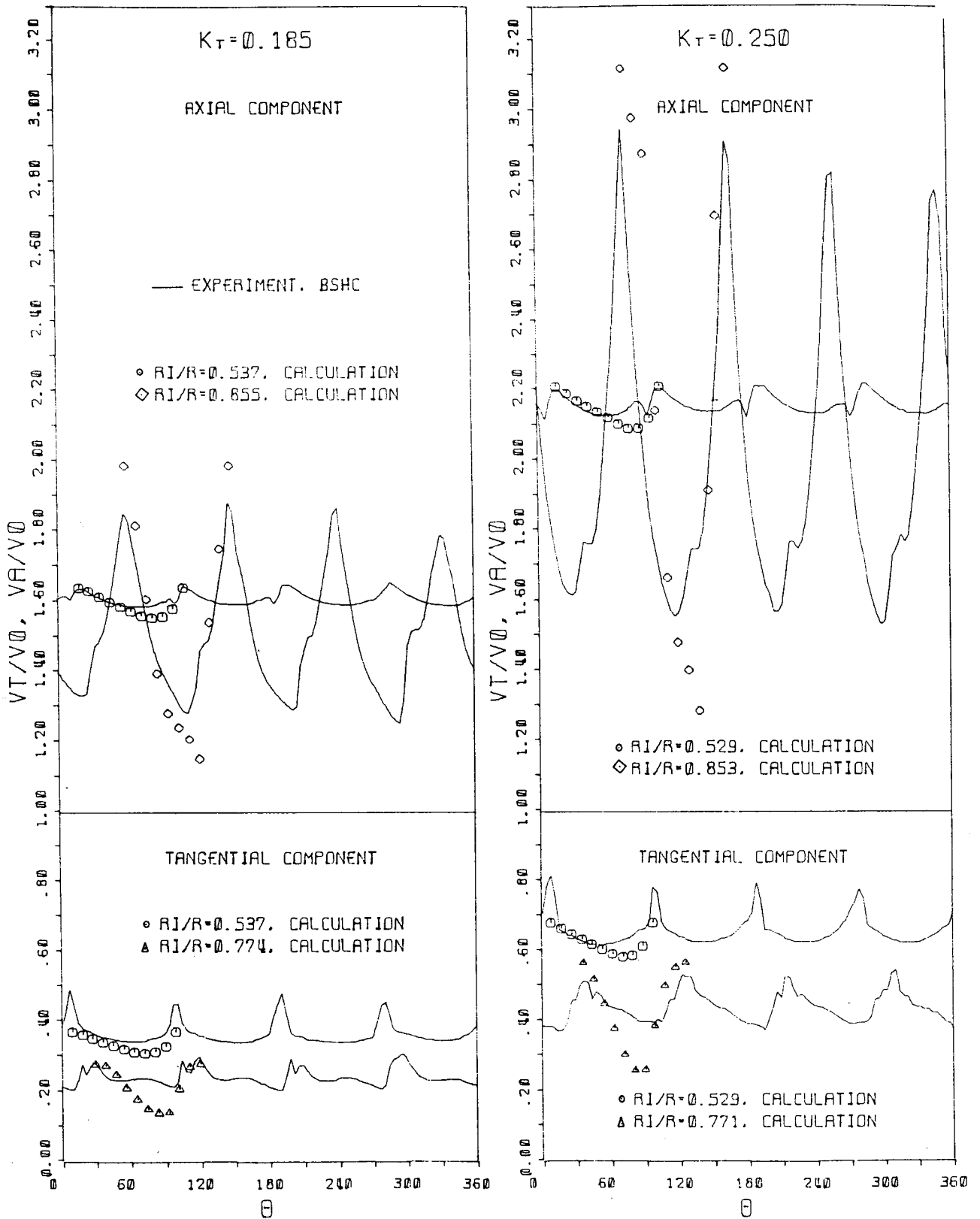


Figure 4 Circumferential variation of axial and tangential velocity at different radii.

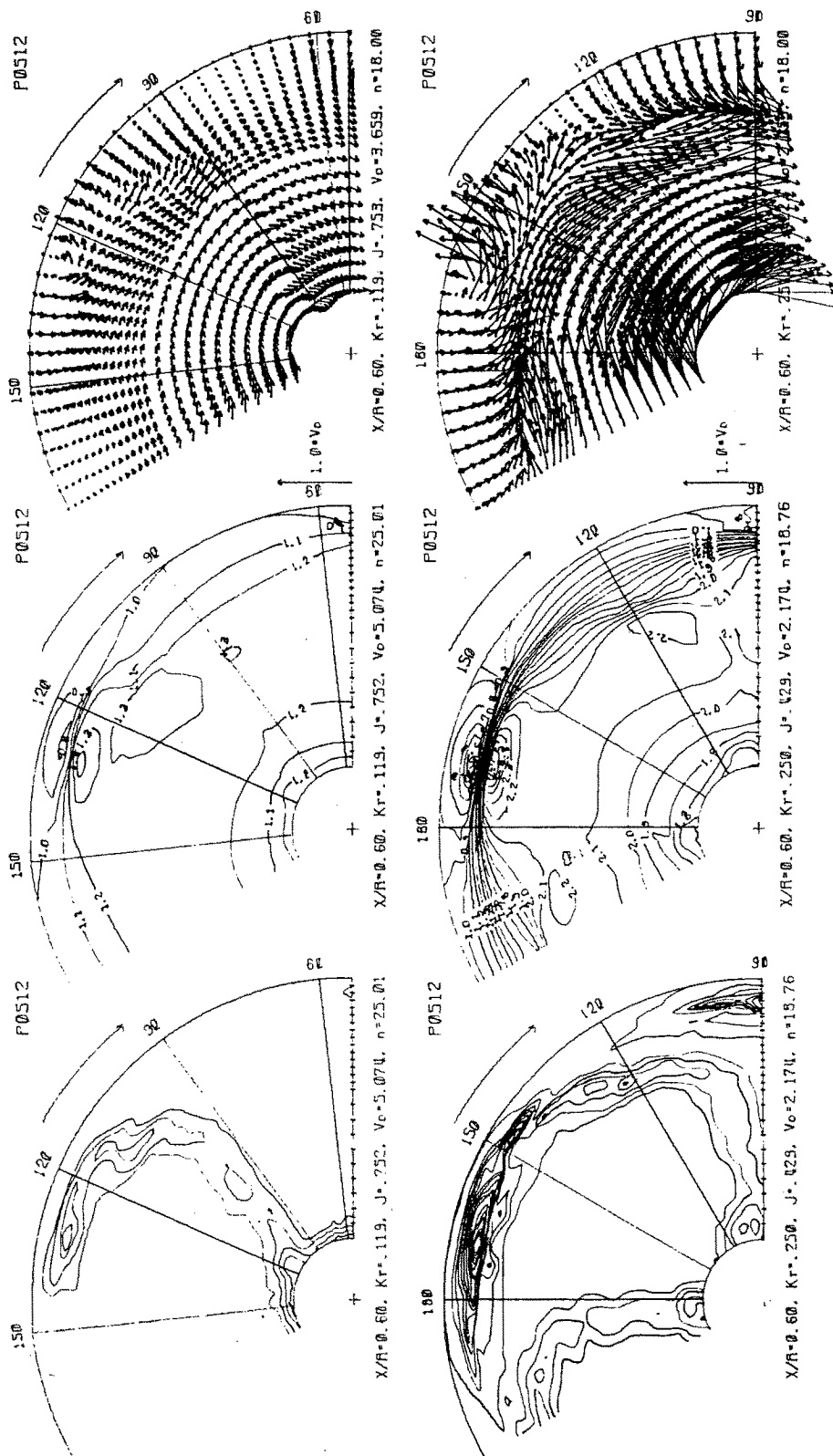


Figure 5 Standard deviation, axial and transverse velocity from LDA measurements for propeller P0152.

#### 4. CONCLUSIONS

The use of deformed slipstream model (without complete rollup), based on exact hydrodynamic relations improves the open-water predictions. The behaviour of the induced velocity is also reasonable as proved by LDA measurements. Special care is required when the induction of tip vortices dominates the flow in order to keep the convergence of the numerical procedure.

#### References

- [1] Glover, E.J., - "A Design Method for Heavily Loaded Marine Propellers". Trans. RINA, Vol. 116, (1974).
- [2] Greely D.S., Kerwin J.E., - "Numerical Method for Propeller Design and Analysis in Steady Flow". Trans. SNAME, Vol. 90, (1982).
- [3] Koumbis A., - "On the Effect of Slipstream on the Mathematical Presentation of Open Propeller". RINA, (1983).
- [4] Wang, G., - "Application of a New Trailing Vortex Wake Model to Propellers". Proc. of 18th ITTC, Vol. 2. pp. 88-92, (1987).
- [5] Hoshino T., Nakamura N., - "Propeller Design and Analysis based on Numerical Lifting-surface Calculations". CADMO 1988.
- [6] Report of Propulsor Committee of the 19th International Towing Tank Conference, 1990, Madrid.
- [7] Varsamov K., Zavadovsky N., Videv T., Haimov A., - "Numerical Design and Performance of Propeller with Complex Blade Shape". SMSSH 1986, Varna, BSHC, (1986).
- [8] Haimov, A., Minchev D., Videv T., - "Off Design Propeller Performance Prediction Based on Deformed Slipstream Model", Proc. of 5th International Congress on Marine Technology, Athens, (1990).
- [9] Kerwin J.E., Lee C.S., - "Prediction of Steady and Unsteady Marine Propeller Performance by Numerical Lifting Surface Theory". Trans. SNAME, Vol. 86, (1978).
- [10] Khadziisky N., Kalchev R., Haimov A., Minchev D., Dimitrov V., - "Analysis of Instantaneous Velocity Field in the Vicinity of a Model Propeller" (to be published), (1990).
- [11] Blaurock J., Lammers G., - "Measurements of Flow Field in the Slipstream of Model Propellers with Different Radial Load Distributions". 3th Intern. Symposium on Laser Anemometry, Winter Annual Meeting of ASME, (1987).

**A. HAIMOV, Z. STANCHEV, I. ANGELOV**  
**Bulgarian Ship Hydrodynamics Centre, Varna,**  
**Bulgaria**

**A FINITE ELEMENT ANALYSIS OF STATIC  
 RESPONSE AND ESTIMATION OF FREE  
 VIBRATIONS OF PROPELLER BLADES**

**1. INTRODUCTION**

The correct treatment of the dynamic structural response of propeller blades involves the hydroelastic problem, especially for complex shaped propellers. Recent publications prove the necessity of combining the hydrodynamic and strength analysis [1,2]. It appeared, however, that the FEM procedure is sensitive to geometry of the blade and the shape and fineness of the computational grid, the choice of the element, the accuracy of the loading distribution and the features of the numerical scheme used. The present work used the conventional approach of dividing the elastic and hydrodynamic problems, the attention being drawn to features of importance also for the full problem. Some peculiarities of the procedure developed for numerical static and free-vibration analysis of the blades are discussed below.

**2. OUTLINE OF THE METHOD**

Here the structural analysis is limited to static response to external loads and computations of free vibrations, the damping being neglected.

The governing equations are respectively:

$$[K] \cdot \{Q\} = \{F\} \tag{1}$$

$$([K] - \Omega^2 [M] + [Mn]) \{q\} = 0 \tag{2}$$

where the following notations are used:

- [K]            stiffness matrix of the blade
- {Q}           displacement vector
- {F}           external load vector
- $\Omega$          natural frequency
- [M]           mass matrix of the blade
- [Mn]         added mass matrix
- {q}           displacement mode vector

Generally, having the external loads from the hydrodynamic analysis and the geometry of the blade, using FEM. Eq.(1) is solved to obtain the static response, i.e. the stresses and deformations. Forming the matrix of masses and calculating the added masses the solution of the eigenvalue problem (2) gives the natural modes and frequencies of the blade.

**3. FEATURES OF THE NUMERICAL SOLUTION**

**3.1. The Finite Element**

The propeller blade is approximated by curved shell type 8-node quadratic superparametric finite element [3]. The nodes defining the geometry are placed on the suction and pressure sides and the nodes for the structural analysis are situated on the camber surface (Fig. 1).

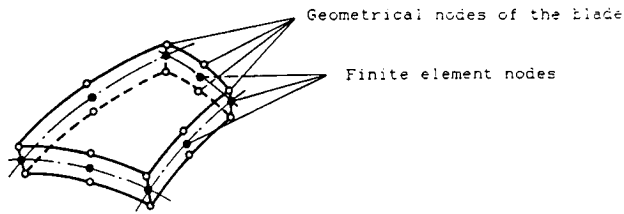


Fig. 1. Sketch of the element

As the stiffness matrix of the element is obtained by numerical integration, the sensitivity of the final results has been analysed, showing better results of the 2-point Gauss-Legendre quadrature for the stiffness matrix compared to the 3-point formula [4]. This is illustrated on Figure 2 for the relative deformation.

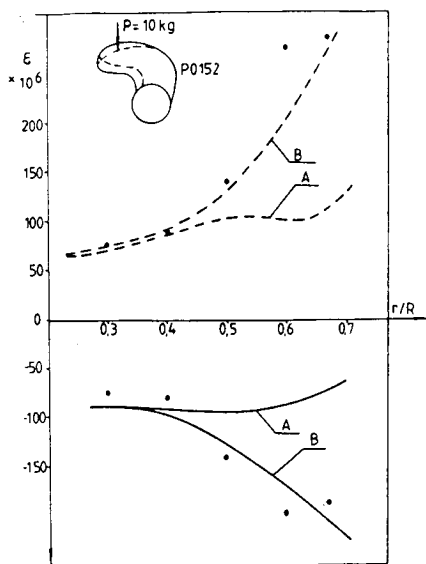


Fig. 2. Relative deformation along a line close to the trailing edge of propeller model PO152 subject to concentrated loading.  
 A - numerical result by 3-point integration  
 B - numerical result by 2-point integration  
 • - experiment for suction side  
 ○ - experiment for pressure side

### 3.2. Propeller Geometry and Mesh Generation

The approach to the mathematical description of propeller blade surfaces is based on a global two-parameter presentation with spline interpolation of the main characteristic elements (see Ref.5), the parameters being the chordwise and radial curvilinear coordinates.

Three types of grids have been created to analyse the sensitivity of the solution to the finesse and shape of the mesh of elements:

- basic cylindrical mesh based on chordwise and radial distribution of nodes;
- isoparametric mesh - keeping approximately equal sides of elements;
- orthogonal mesh formed by crossing the lines of equal chordwise position points with orthogonal lines;

Example of two meshes on a highly skewed blade is shown in Figure 3. Figure 4 presents results for the ITTC comparative example [6], computed for two grids. Better results are obtained with the izoparametric or orthogonal mesh explained by the regularity of the shape of elements.

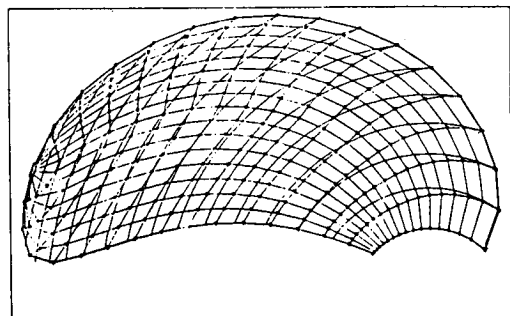


Fig. 3. Cylindrical and isoparametric mesh on the blade of ITTC propeller [6].

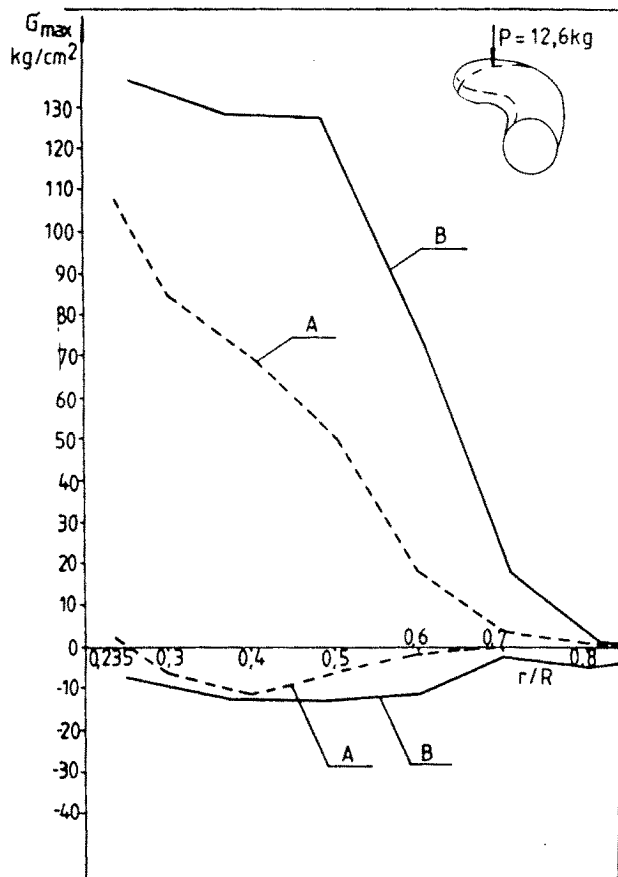


Fig. 4. Calculated principal stresses along a line close to the trailing edge of ITTC propeller model subject to concentrated loading.  
 A - regular cylindrical mesh  
 B - isoparametric mesh

### 3.3 Static Hydrodynamic Loading on the Blade

The loading distribution together with geometrical data is prepared automatically as input for the strength computer program by the hydrodynamic performance prediction program. The lifting surface method is used of continuous vorticity distribution giving the pressure jump attributed to the camber surface. Details of this method developed for highly skewed propellers can be found in Ref.5

### 3.4. Mass Matrix

The mass of the blade is distributed over the nodes of the element following the static condensation principle.

The approach adopted for consideration of added masses is based on the results of dynamic tests in air and water [7], showing close resemblance of the shape of the free vibration modes. Thus, for the first harmonic, the estimation of added masses is based on rigid body displacements, obtaining diagonal form of the matrix.

As was confirmed by the results, the longitudinal added mass computed by approximate formula [8] is sufficient for reasonable estimation of the first mode of free vibrations in water.

## 4. VALIDATION AND RESULTS

The algorithm and computer codes have been validated first on analytical solution for a plate by comparison of displacements due to concentrated load showing less than 0.5 % difference.

It was found that reducing the number of nodes of numerical integration and improving the shape of the elements decreases the sensitivity of the precision to change of geometry and number of elements.

The comparison with experiments and other calculations is performed for conventional propeller (Fig. 5, the experiment is from [9]) and for high-skew propeller model PO152 (Fig. 6 & 7, BSHC experiment). Comparison is also done with ITTC model [6], Boswell and others for the steady structural response at concentrated loads.

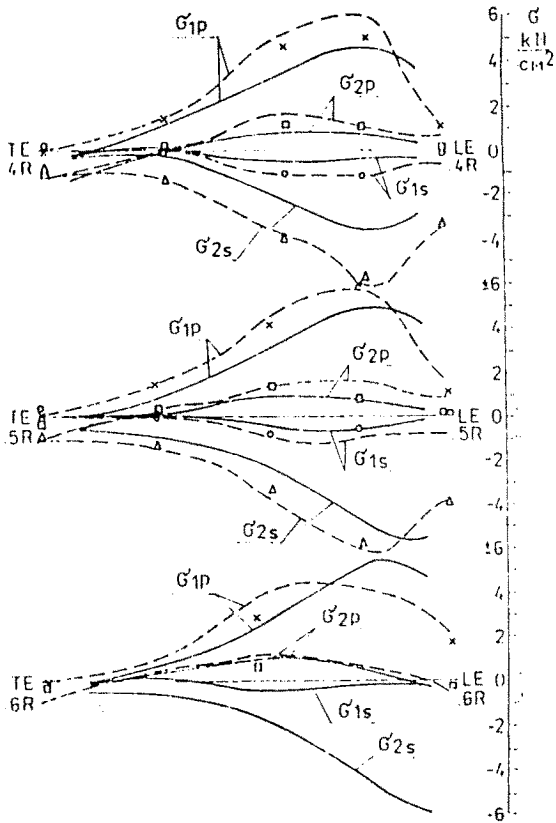


Fig. 5. Experimental and numerical principal stresses for loading case 3. [9].

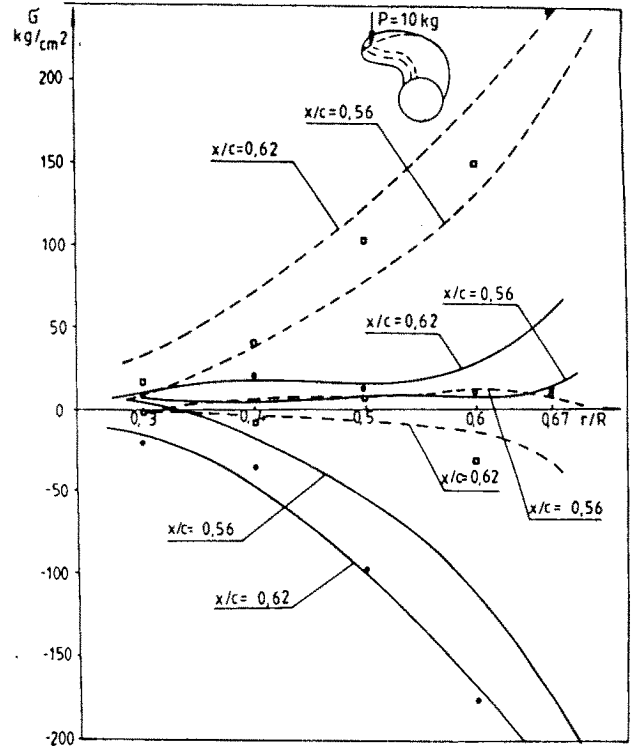


Fig. 7. Calculated and measured principal stresses on the blade of propeller PO152 for concentrated loading at  $r=0.8$ ,  $x/c=0.95$ .

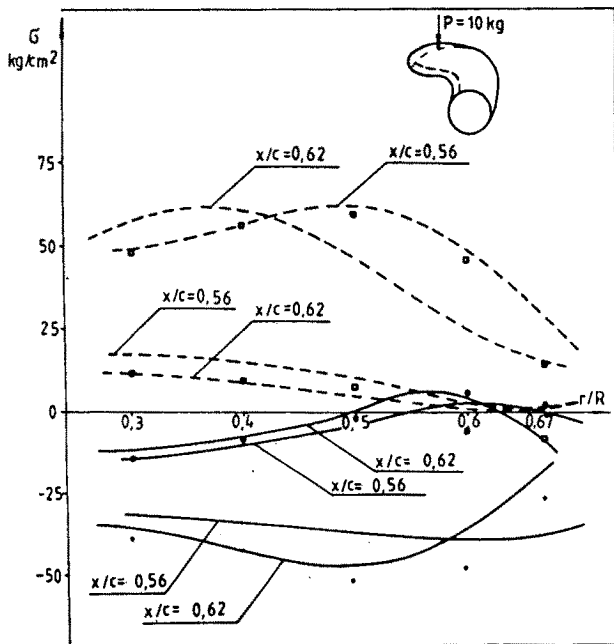


Fig. 6. Calculated and measured principal stresses on the blade of propeller PO152 for concentrated loading at  $r=0.8$ ,  $x/c=0.05$ .

BSHC free vibration test results [7] in air and water are compared to computational in Table 1.

Table 1 Numerical and Experimental Natural Frequencies for Propeller Model Blade PO152

Fluid	Harmonic N <sup>o</sup>	Numerical	Experimental
Air	1	337	313
	2	756	698
	3	1062	1030
Water	1	207	210

## 5. CONCLUSIONS

The complex shape of the propeller blades, including considerable thickness change require appropriate finite element and numerical scheme to obtain accurate results. The steady strength results for high-skew and raked propellers are sensitive to the type of mesh used. For very high skew some underestimate of the stresses is observed when using the basic grid, in other cases the method being satisfactory. The lack of published results for the natural frequencies of propeller blades limited the comparison to one case with very good coincidence even for water (first harmonic), taking into account only the rigid body longitudinal added mass.

### References

- [1] Koronowicz T., Kaczorowski J., - "Hydroelastic Effects in Highly-Skewed Propellers". Proc. of PRADS 1989. Vol. 1., Pap. 15, BSHC, Varna.
- [2] Nho I., Lee C.-S., Kim M.-C., - "A Finite Element Dynamic Analysis of Marine Propeller Blades". Proc. of PRADS 1989. Vol. 3. Pap. 114, BSHC, Varna.
- [3] Stanchev Z., "Strength Calculations of Propellers of Complex Shape Blades Using Finite Elements". Voprosy Sudostroeniya, Vol. 39 (in Russian), (1984).
- [4] Angelow, I., Simow St., Stantschew Z., Konaktschiewa I., "Zur Berechnung des Spannungs- und Deformationszustandes in Propellerflugen mit Finiten Schalenelementen". Sonderheft Internationales Rostocker Schiffstechnisches Symposium, Band 2, (1989).
- [5] Varsamov K., Zavadovsky N., Videv T., Haimov A., - "Numerical Design and Performance of Propeller with Complex Blade Shape". SMSSH 1986, Varna. BSHC.
- [6] Report of Propulsor Committee of 18th ITTC, 1987. Kobe. pp. 139-141.
- [7] Angelov I., Simov S., Haimov A., - "Static and Vibration Tests of Propeller Models". Annual Publications of the Institute for Shipbuilding, Varna. To be published in Bulgarian.
- [8] Korotin A., - "Added Masses of Ships". Sudostroenie Publ. House., Leningrad (in Russian), (1986).
- [9] Beek G.H.M., - "Calculation of Propeller Blade Stresses and Comparison with Test Results". ISP, Vol. 24, No. 277, (1977).

PS-2.3

THIS THEORY APPLIES TO:

- NOMINAL WAKES OF SHIP HULLS WITHOUT SEPARATION
- LIGHT-TO-MODERATE PROPELLER LOADINGS
- A PRACTICAL CLASS OF SHEAR FLOWS
- INVISCID, INCOMPRESSIBLE FLUIDS
- $U(r) \neq 0$

J. P. BRESLIN

Professor Emeritus, U.S.A.

AN ANALYTICAL THEORY OF PROPELLER-GENERATED EFFECTIVE WAKE

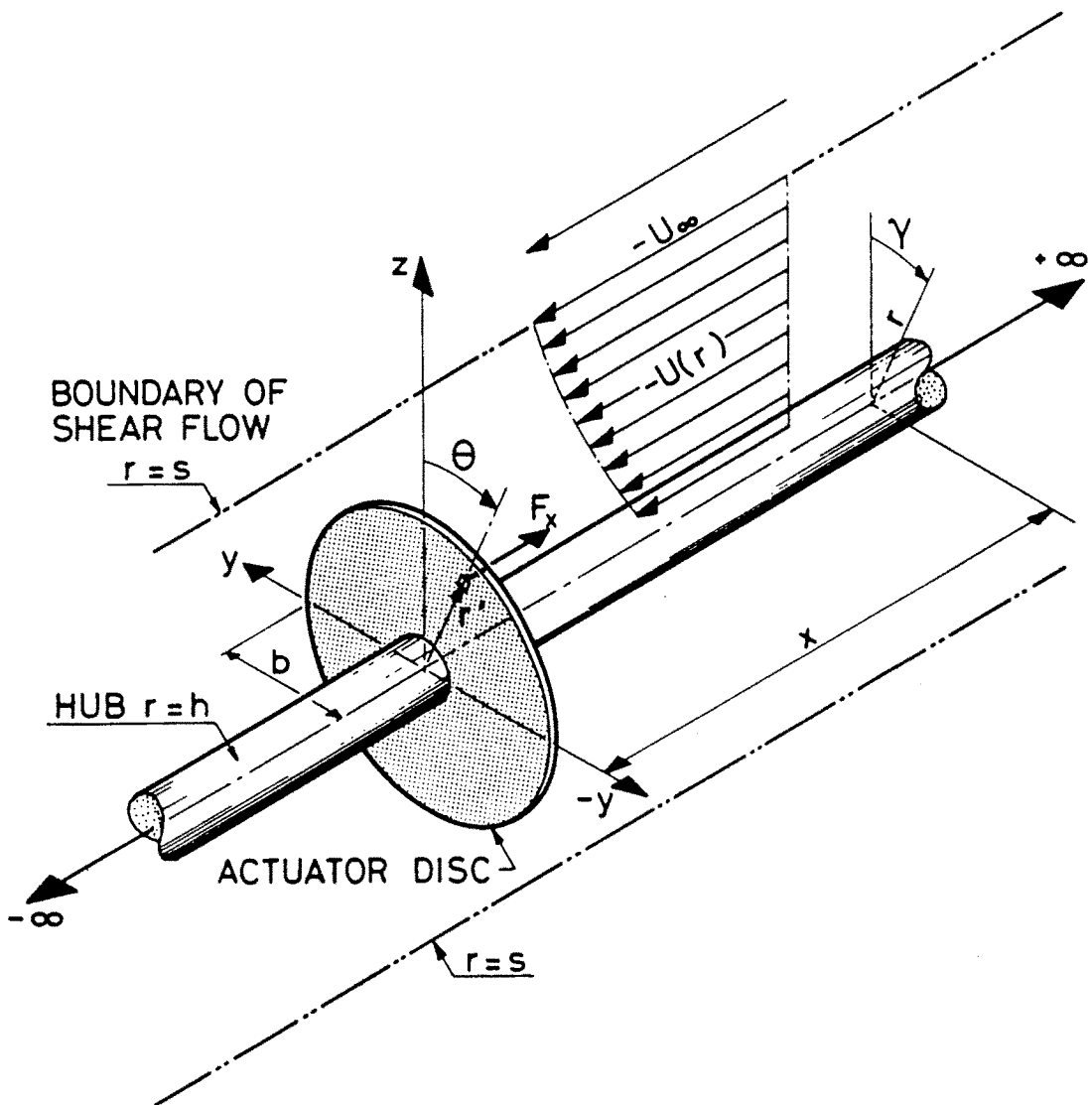


FIG. 1. ACTUATOR DISC REPRESENTATION OF A PROPELLER IN AN AXISYMETRIC SHEAR FLOW  $-U(r)$ .

LINEARIZED AXISYMMETRIC EULER EQUATIONS WITH RADIAL SHEAR

$$-\bar{U}(r) \frac{\partial u'}{\partial x} - \underbrace{\frac{d\bar{U}}{dr}(r) \cdot w'}_{\text{SHEAR COUPLING}} + \frac{1}{\rho} \frac{\partial p'}{\partial x} = \frac{-F_x}{\rho} \quad (1)$$

$$-\bar{U}(r) \frac{\partial w'}{\partial x} + \frac{1}{\rho} \frac{\partial p'}{\partial r} = 0 \quad (2)$$

CONTINUITY

$$\frac{\partial u'}{\partial x} + \frac{\partial w'}{\partial r} + \frac{w'}{r} = 0 \quad (3)$$

where 
$$\bar{U}(r) = \frac{1}{2\pi} \int_0^{2\pi} U(r, \gamma) d\gamma$$

THE ZERO HARMONIC OF THE AXIAL NOMINAL WAKE

$$F_x = \Delta p(r') \delta(x) \delta(r-r') \frac{dS'}{2\pi}$$

FORCE DENSITY ON ELEMENT OF THE

ACTUATOR DISC;  $\delta(\ ) =$  DIRAC DELTA FUNCTION

ELIMINATING  $u'$  and  $w'$

$$\nabla_2^2 p' - \underbrace{\frac{2}{U(r)} \frac{d\bar{U}}{dr}(r) \frac{\partial p'}{\partial r}}_{\text{SHEAR TERM}} = -\frac{\Delta p}{2\pi} \frac{d\delta(x)}{dx} \delta(r-r') dS'; \quad (4)$$

$$\nabla_2^2 = \frac{\partial^2}{\partial x^2} + \frac{\partial^2}{\partial r^2} + \frac{1}{r} \frac{\partial}{\partial r}$$

A TRANSFORMATION

$$\psi = V(r) p'(x, r); \quad V(r) = \frac{1}{\bar{U}(r)} \quad (5)$$

EXACTLY CONVERTS (4) TO

$$\nabla_2^2 \psi - \underbrace{\frac{1}{V} \nabla_1^2 V}_{\text{SHEAR TERM}} \cdot \psi = -\frac{\Delta p(r')}{2\pi} V(r) \frac{d\delta(x)}{dx} \delta(r-r') dS'$$

where 
$$\nabla_1^2 = \frac{d^2}{dr^2} + \frac{1}{r} \frac{d}{dr}$$

DIFFICULT TO SOLVE FOR ARBITRARY

$$V(r) = \frac{1}{\bar{U}(r)}$$

A CLASS OF SHEAR FLOWS

ASSUME

$$\frac{\nabla_1^2 V(r)}{V(r)} = k^2, \text{ a constant} - \quad (6)$$

or

$$\frac{d^2 V}{dr^2} + \frac{1}{r} \frac{dV}{dr} - k^2 V = 0 \quad (7)$$

SOLUTION:

$$V(r) = A I_0(kr) + B K_0(kr) \quad (8)$$

$= \frac{1}{\bar{U}(r)}$ ;  $I_0, K_0$  ARE MODIFIED BESSEL FUNCTIONS OF 1st & 2nd KIND OF ORDER ZERO

QUESTION:

CAN A.B. & k BE DETERMINED SO THAT  $V^{-1}$  CLOSELY FITS

MEASURED NOMINAL WAKES OVER

ENTIRE REGION OF PROPELLER DISC?

ANSWER: YES. FOR SURFACE-SHIP AND

SUBMARINE MODELS

DEMONSTRATIONS IN FIGS 2.3.4

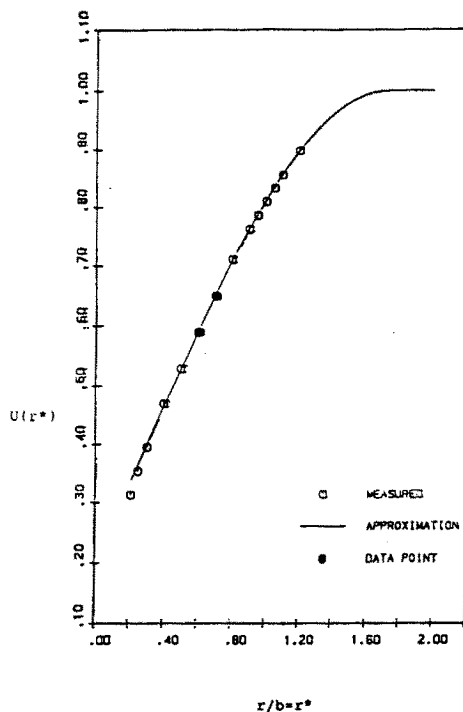


FIG. 2. COMPARISON OF MEASURED NOMINAL WAKE 1 AND FIT OF  $\bar{U}(r)$  FROM EQUATION 8 TO MEASURED VALUES

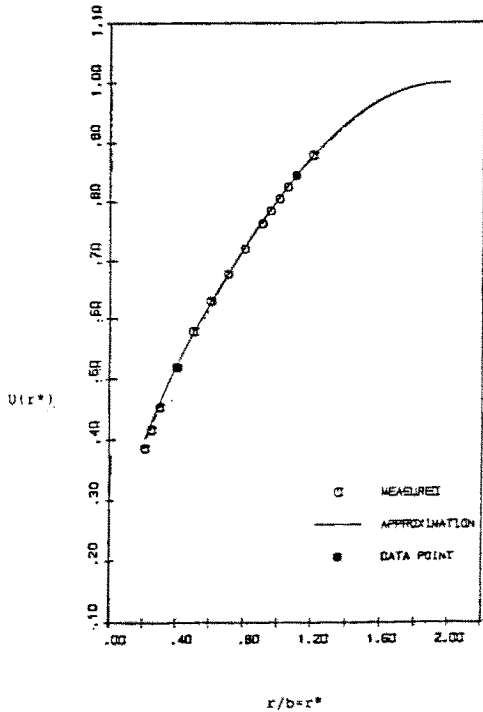


FIG. 3. COMPARISON OF MEASURED NOMINAL WAKE C AND FIT OF  $\bar{U}(r)$  FROM EQUATION 8 TO MEASURED VALUES

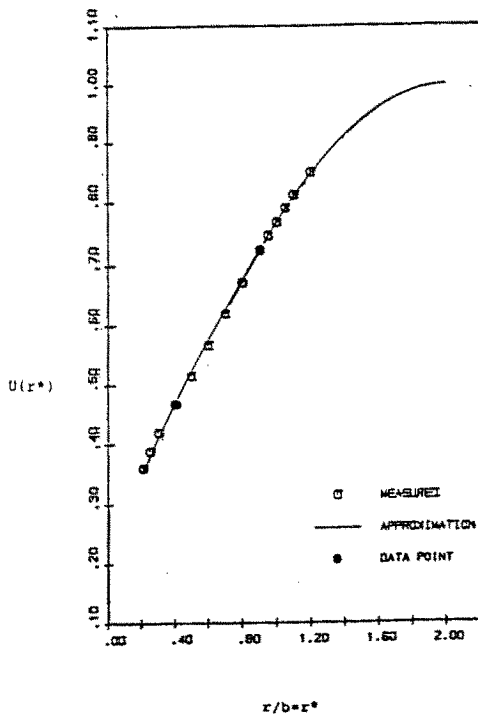


FIG. 4. COMPARISON OF MEASURED NOMINAL WAKE D AND FIT OF  $\bar{U}(r)$  FROM EQUATION 8 TO MEASURED VALUES

SOLUTION FOR PRESSURE AND VELOCITY FIELDS FOR THE CLASS OF SHEAR FLOW

EQUATION (6) REDUCES TO:

$$(v_2^2 - k^2)\psi = -\frac{\Delta p}{2\pi} V(r) \frac{d\delta(x)}{dx} \delta(r-r') ds' \quad (9)$$

For  $h \leq r \leq s$

AND TO

$$v_2^2 \psi_0 = 0 \quad ; \quad \text{For } s \leq r < \infty \quad (10)$$

IN THE OUTER REGION OF ZERO SHEAR

FOURIER INTEGRAL TRANSFORMED EQUATIONS ARE SOLVED TO GIVE

$$\tilde{\psi}_0 = \hat{a}(\xi) K_0(|\xi|r) \quad ; \quad s \leq r < \infty \quad (11)$$

$$\tilde{\psi} = \hat{b}(\xi) I_0(\lambda r) + \hat{c} K_0(\lambda r) \quad ; \quad h \leq r \leq s \quad (12)$$

$$\lambda = \sqrt{\xi^2 + k^2} \quad ; \quad \xi, \text{ the F.I.T. parameter}$$

$\hat{a}, \hat{b}, \hat{c}$  ARE UNKNOWN COEFFICIENTS

THREE (3) PHYSICAL CONDITIONS

ARE ENFORCED TO EVALUATE THEM

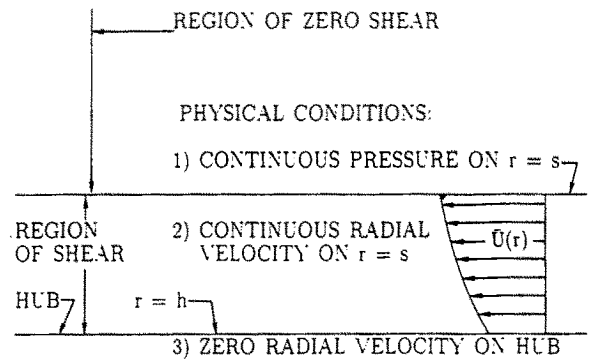


FIG. 5 PHYSICAL CONDITIONS IMPOSED ALONG BOUNDARIES OF SHEAR FLOW

These CONDITIONS TRANSLATE TO

$$\tilde{\psi}(s) = \tilde{\psi}_0(s)$$

$$\frac{\partial \tilde{\psi}(s)}{\partial r} = \frac{\partial \tilde{\psi}_0(s)}{\partial r}$$

$$\left. \frac{d}{dr} (\bar{U}(r) \tilde{\psi}(r)) \right|_{r=h} = 0$$

$\hat{a}, \hat{b}, \hat{c}$  are completely determined.

w and then u are obtained by

integration of the linearized Euler Equations

Results are shown in Figures 6, 7 and 8

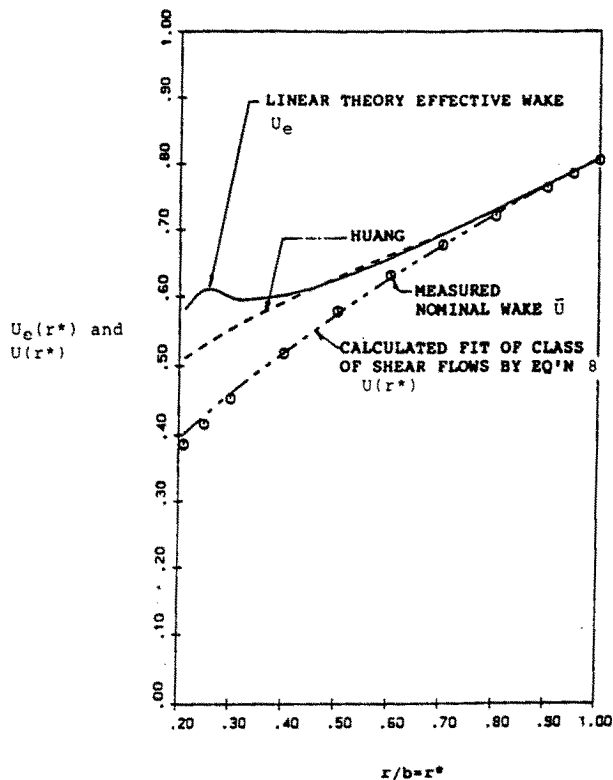


FIG. 6. NOMINAL AND EFFECTIVE WAKES WITHIN THE PROPELLER DISC (FOR HUANG'S WAKE C AND  $C_T=0.356$ )

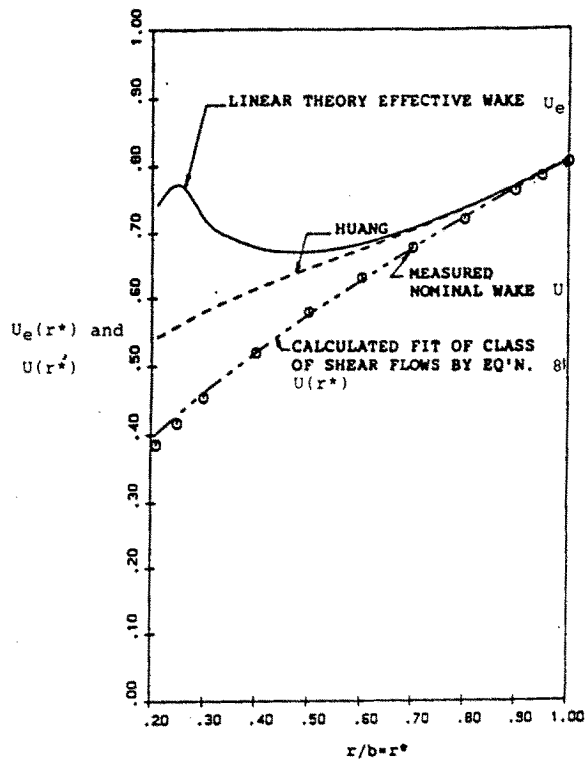


FIG. 8. NOMINAL AND EFFECTIVE WAKES WITHIN THE PROPELLER DISC (FOR HUANG'S WAKE C AND  $C_T=0.676$ )

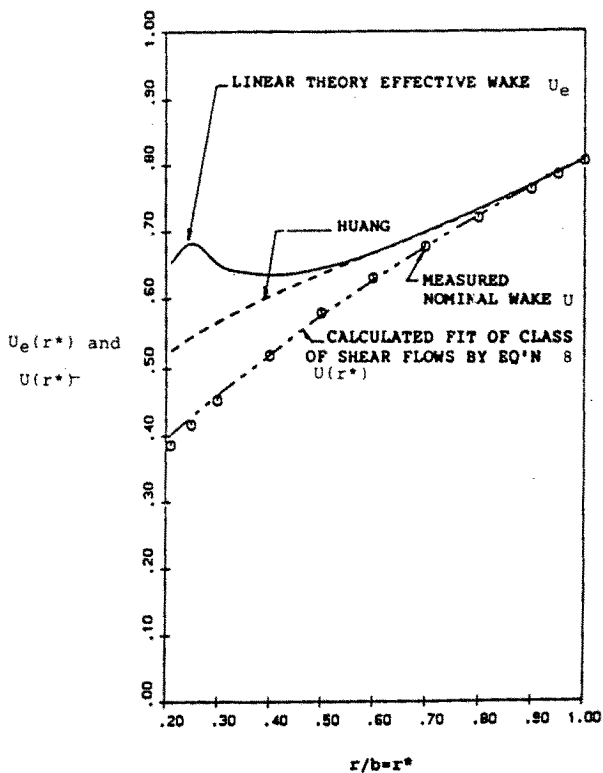


FIG. 7. NOMINAL AND EFFECTIVE WAKES WITHIN THE PROPELLER DISC (FOR HUANG'S WAKE C AND  $C_T=0.498$ )

PARTLY NON-LINEAR THEORY

NON-LINEAR EFFECTS IN AXIAL COMPONENT SET IN AT  $C_T$  0.20 IN ABSENCE OF SHEAR

EXCURSION OF LINEAR THEORY AT SMALL RADII IS BELIEVED DUE TO:

NON-LINEAR INDUCTION  
ABSENCE OF HUB

RETAINING  $u' \frac{\partial u'}{\partial x}$  IN AXIAL EQUATION

BUT NEGLECTING NON-LINEAR TERMS IN RADIAL EQUATION AND USING LINEARIZED SOLUTION FOR PRESSURE A PARTLY NON-LINEAR INCREMENT DUE TO SHEAR IS FOUND TO BE (ON THE DISC).

$$\left[ U_s \right]_{pn-1} = \bar{U}(r) \left\{ \sqrt{1 + \frac{\Delta p'(r)}{\bar{U}^2(r)}} - \sqrt{1 + \frac{\Delta p'(r)}{\bar{U}^2(r)} - \frac{2U_s}{\bar{U}(r)}} \right\};$$

where 
$$U_s = \frac{\bar{U}'}{\rho \bar{U}^2(r)} \int_0^\infty dx'' \int_{x''}^\infty dx' \frac{\partial p}{\partial r}(x', r)$$

The LINEARIZED INCREMENT DUE TO SHEAR

**THE PARTLY NON-LINEAR EFFECTIVE WAKE**

is (WITHOUT HUB)

$$[U_e]_{pn-1} = -U(r) + [U_s]_{pn-1}$$

GRAPHS IN FIGURES 9 AND 10 SHOW COMPARISON WITH HUANG INDICATING MUCH BETTER AGREEMENT ALTHOUGH EFFECT OF HUB BOUNDARY CONDITION IS NOT INCLUDED

COMPARISON OF RATIOS OF "MEASURED" WAKE USING PROPELLER CHARACTERISTICS AND MEAN OF LINEARIZED THEORY

NOMINAL WAKE	$C_T$	MEAS. 'D (1-W <sub>T</sub> ) CALCULATED	
		BRESLIN	HUANG
1	0.370	1.006	1.013
1	0.654	0.975	1.008
C	0.356	0.994	1.000
C	0.498	0.990	1.007
C	0.676	0.971	1.003
D	0.360	1.018	1.039
D	0.500	0.973	1.040
D	0.706	0.991	1.036

LINEAR THEORY VERY GOOD UP TO  $C_T = 0.6$

PARTLY NON-LINEAR THEORY EXPECTED TO BE ACCURATE OVER  $0 < C_T < 1.0$

**CONCLUSIONS**

- THIS THEORY IS ADEQUATE TO PREDICT EFFECTIVE WAKE FROM EXISTING NOMINAL WAKE FOR MODELS OF FINE FORM HULLS WITHOUT SEPARATION
- THE ALTERATION OF RADIAL LOADING DUE TO EFFECTIVE WAKE AND SUBSEQUENT EFFECT OF THIS ON EFFECTIVE WAKE HAS NOT BEEN DETERMINED
- APPLICATION OF THIS CLASS OF SHEAR FLOWS TO MANY WAKE MEASUREMENTS SHOULD BE DONE AS A COMPACT REPRESENTATION OF SUCH DATA

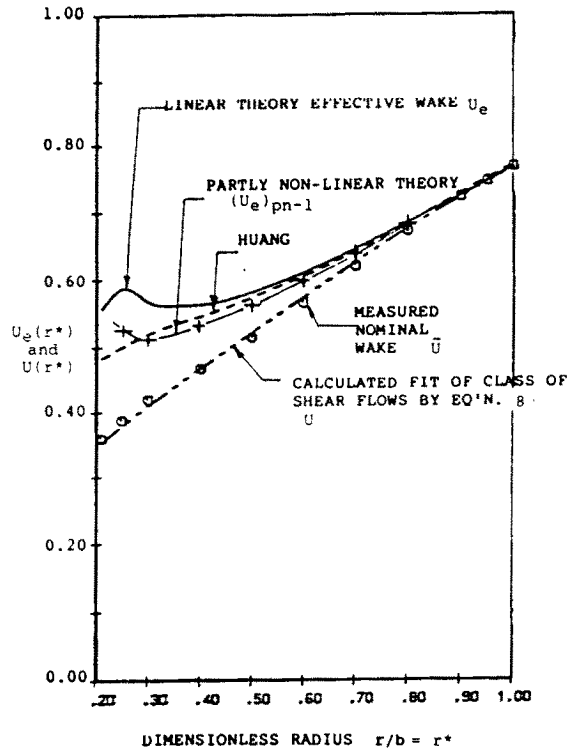


FIG.9 NOMINAL AND EFFECTIVE AXIAL WAKES WITHIN THE PROPELLER DISC

(For Huang's Wake D and disc loading  $C_T = 0.360$ )

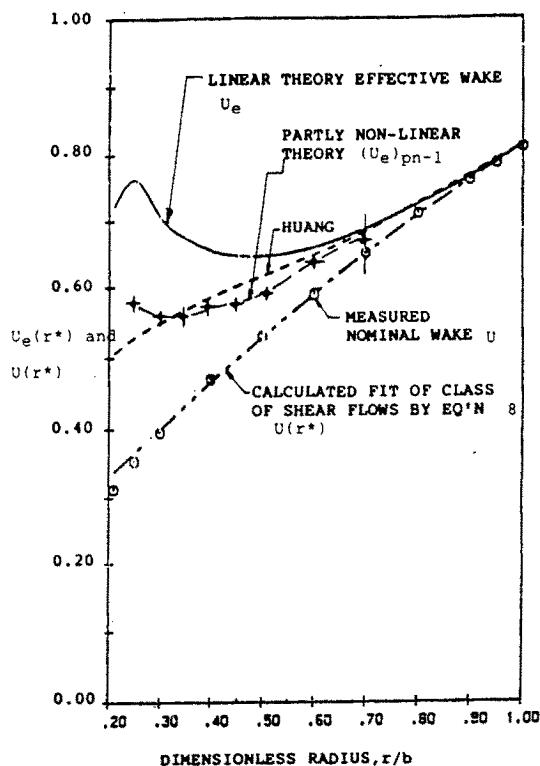


FIG.10 NOMINAL AND EFFECTIVE AXIAL WAKES WITHIN THE PROPELLER DISC

(For Huang's Wake 1 and  $C_T = 0.654$ )

**CHEN-WEN JIANG, HAN-LIEH LIU, T.T.  
HUANG**

**David Taylor Research Center, Bethesda, U.S.A.**

**DETERMINATION OF WIND TUNNEL WALL  
EFFECTS AND CORRECTIONS**

ABSTRACT

Detailed velocity and pressure measurements and numerical computations are used to determine the effects of wind tunnel walls on the flow field of an axisymmetric ship model. The large wind tunnel used has a closed jet test section followed by an open jet section. The tunnel walls are simulated by panels in a potential-flow computer code. The zero normal velocity boundary condition is imposed on the wall panels of the closed jet, and the constant pressure condition is satisfied on the boundary panels of the open jet (by iterative computation). A viscous-inviscid boundary layer inter-action procedure is used to compute the flow on the axisymmetric ship model. The measured and computed velocity and static pressure across the entire plane at 85% body length are found to be uniform with and without the tunnel walls. However, the velocity inside the tunnel is higher than the free-flight condition. The computed or measured static pressure coefficients and velocity distributions based on the computed or measured reference velocity and static pressure in the plane of 85% body length at the point of 3.6 maximum body radius from the body axis indicate that the tunnel wall blockage effect can almost be eliminated by using these reference velocity and static pressure val-

ues. The measured variations of the velocity distributions across in-flow and out-flow planes are found to be uniform within 0.5% of the reference velocity. Longitudinal flow variation along the tunnel is also measured and documented. When the blockage corrections are applied, the flow field measured inside the tunnel simulates the free-flight condition satisfactorily if the overall blockage ratio is less than 10 .

1. INTRODUCTION

It is desirable to use the largest model in a wind or a water tunnel to obtain flow field data at high Reynolds numbers. The wind tunnel blockage effect due to the constraint of the tunnel walls increases with model size. If the blockage effect can be quantified and blockage corrections can be found, then the corrected data obtained in a tunnel having moderate blockage shall simulate the free flight conditions at high Reynolds numbers. A simple numerical computation method will be used to demonstrate that the measured blockage effect can be quantified and a simple blockage correction can be found to remove the wall effects from the measured data.

## 2. WIND TUNNEL AND MODEL

The experimental investigation of the wind tunnel wall effects on an axisymmetric model was conducted in the David Taylor Research Center Anechoic Flow Facility (DTRC AFF). As shown in Figure 1, the wind tunnel has a closed jet test section that is 2.4 m (8 ft) square and 4.19 m (13.75 ft) long. The corners have 0.534 x 0.534 m (1 ft 9 in. x 1 ft 9 in.) fillets which are carried through the contraction. Allowance for boundary layer growth along the tunnel is made by tapering the corner fillets, starting from 0.534 x 0.534 m (1 ft 9 in. x 1 ft 9 in.) at the test section entrance to 0.509 x 0.509 m (1 ft 8 in. x 1 ft 8 in.) at the test section exit. The test section is followed by a large acoustically-lined chamber 7.16 m (23.5 ft) square, normal to the flow, and 6.40 m (21 ft) long. The forebody and most of the parallel middle body of the model are located in the closed-jet test section, and the afterbody is protruding into the open-jet anechoic chamber as shown in Figure 2.

The axisymmetric hull is made of molded fiberglass. The hull is reinforced with a 0.25 m (10 in.) wide U-channel as its strongback. The model is supported by two thin NACA-0015 struts located at  $x/L = 0.24$  and  $0.63$ , respectively. The two supporting struts have a 15 cm (6 in.) chord. The strut bases are mounted below the tunnel floor for minimal flow disturbance. The model end of the strut is connected to a gimble secured to the model strongback. Actual velocity surveys behind the supporting struts indicates that the wake data is free from strut wake contamination except in the immediate neighborhood of the strut

defined by  $\pm 30^\circ$  from the strut centerlines. The axisymmetric hull has an overall length  $L$  of 4.356 m (14.292 ft) and a maximum diameter  $D$  of 0.508 m (1.667 ft). The hull is composed of a forebody of length 1.016 m (3.333 ft), a parallel middle body section of length 2.229 m (7.313 ft), an afterbody of length 1.111 m (3.646 ft), and an afterbody cap of length 0.095 m (0.313 ft). This model is designated as DTRC Model No. 5471. Detailed descriptions of pretest analysis and setup are given in reference [1].

## 3. NUMERICAL SIMULATION OF THE MODEL IN THE TUNNEL

A potential-flow method, the panel code computer program VSAERO [2], with viscous flow correction [3, 4] has been used to compute the flow field in the AFF. In this numerical simulation, only the bare axisymmetric body with the two supporting struts are modeled.

Figure 3 depicts the grid representation of the axisymmetric model. The two dense grid regions are the positions where the struts are located in the closed tunnel. The model was positioned along the axis in the AFF tunnel, with the inlet at 1.52 m (5 ft) ahead of the bow and the outlet at 1.44 m (4.71 ft) after the stern of the model. A uniform flow field was assumed at the inlet and the outlet. Figure 4 shows the pressure coefficient distribution along the model representing the blockage effect in the AFF tunnel due to the presence of the model. As shown in Figure 4, the overall tunnel blockage can be estimated as the average difference in the values of  $C_p$  over the body length. This difference in  $C_p$  is about

0.05 and hence the difference in velocity is about 0.025.

Because of the relatively large size of the model, the forward section of the model was positioned in the closed tunnel section while the model stern extended into the open jet section of the tunnel. To estimate this effect, a free surface boundary condition was assumed in the tunnel jet region to predict the pressure coefficient along the model. Velocity components in the flow direction on the panels of the open-jet region were iterated to achieve a constant value by imposing different normal velocities on the tunnel panels in the open-jet region. In order to simplify the iteration procedure, an equivalent circular area of the tunnel was used in the computation. Both the model and the tunnel were axisymmetric so that the free surface was also axisymmetric. The panel representation of the model and the tunnel is shown in Figure 5. In order to iterate for the constant pressure condition along the free surface of the jet, normal velocities were specified in the VSAERO calculation over the last one-third of the tunnel panels. Figure 6 demonstrated that the jet region has a small influence on the surface pressure calculation near the stern. The open-jet flow tends to locally follow earlier open flow condition calculations.

Since only a small portion of the model was in the open jet and the computed effect of the free surface of the open jet on the values of  $C_p$  was small, further simulation of the open jet was not deemed necessary.

The tunnel velocity and static pressure are expected to vary along the body and

across the tunnel section. Since viscous effects are important in the model stern region, the panel code has been modified to include the boundary-layer displacement thickness computed from the modified Douglas Cebeci-Smith axisymmetric boundary layer program [3,4]. This viscous inviscid procedure is used to compute velocity and static pressure variations in the tunnel. The computed velocity variations along the upper body meridian with and without the presence of the tunnel walls are shown in Figures 7a and 7b at three radial positions measured from the body axis.

As shown in Figure 7, the computed axial velocity distributions at different radii are crossing each other at the entire  $x/L = 0.85$  plane. The presence of tunnel walls causes a 2.4% increase of axial velocity and a 4.8% of static pressure. Detailed velocity and static pressure measurements were made inside the tunnel with the presence of the axisymmetric body. It was found that, at this  $x/L = 0.85$  plane, the velocity variation was less than 0.5% and the static pressure coefficient variation was less than 1.0%. The velocity and static pressure at this plane were then used as the tunnel reference free stream and static pressure. Specifically, two pitot probes, mounted at  $x/L = 0.85$  and  $r/R_{max} = 3.6$  as shown in Figure 2, were used to measure and monitor the tunnel reference velocity and static pressure for all the experiments, where  $r$  is the radial distance from the model axis and  $R_{max}$  is the maximum radius of the model. The computed static pressure coefficient based on the computed reference velocity and static pressure at  $x/L = 0.85$  with and without the tunnel walls

are shown in Figure 8. Figure 8 indicates that the tunnel blockage effect can almost be eliminated by using the computed reference velocity and static pressure at  $x/L = 0.85$ . Therefore, all the measured velocities and static pressures are normalized by the measured reference velocity and static pressure at  $x/L = 0.85$  and  $r/R_{max} = 0.36$ .

#### 4. CONDITIONS OF IN-FLOW AND OUT-FLOW PLANES

The in-flow plane may be selected at  $x/L = -0.45$ , where there is no difference in the computed axial velocity with and without the model in the tunnel. The measured variation of the axial velocities across the in-flow plane of the empty tunnel was found to be  $0.5\% U_{ref}$ .

The out-flow plane may be selected at  $x/L = 1.2$ , where the difference in measured axial velocities with and without the model in the tunnel is about  $0.5\% U_{ref}$ . The measured variation of the axial velocities across the out-flow plane of the empty tunnel was found to be  $0.5\% U_{ref}$ . Therefore, the in-flow and out-flow at  $x/L = -0.45$  and  $1.2$ , respectively, can be considered uniform.

#### 5. LONGITUDINAL FLOW VARIATION ALONG THE TUNNEL

The measured variations of tunnel velocity and static pressure along the tunnel ceiling at  $r/R_{max} = 3.6$  with and without the model are shown in Figures 9 and 10. A small favorable pressure gradient accompanied by a small velocity

gradient along the tunnel is observed. In the closed-jet test section, the measured static pressure coefficient gradient, caused mainly by the viscous friction, is found to be  $0.003$  per foot of the model length. The measured non-dimensional tunnel velocity  $u(x)/U_{ref}$  increase is less than  $0.002$  per foot of model length for  $x/L < 0.7$ . The variations of velocity and static pressure at the stern section where  $x/L > 0.7$  are negligibly small. Figure 11 shows the comparison of measured and computed velocities along the tunnel axis. At the three measured radial positions from the model axis, the measured velocities normalized with the reference velocity at  $x/L = 0.85$  are lower than the computed values for  $x/L < 0.7$ . However, the measured velocities normalized with the local velocities of the empty tunnel are very close to the computed values. Similarly, the measured tunnel static pressure coefficients (Figure 10) subtracted from the actual tunnel static pressure coefficients, the corrected static pressure coefficients along the tunnel, agree well with the computed values (Figure 12). Figure 13 presents the computed and measured surface pressure coefficients on the model. When the longitudinal pressure variation is removed from the measured data, the corrected pressure coefficient data agree well with the computed values where no pressure variation is imposed in the computation. Figure 14 gives the computed and measured velocity profiles at  $x/L = 0.927$  and  $0.978$ , respectively. Good agreement is achieved when the velocities are normalized by the reference velocity. These good comparisons demonstrate that the tunnel effects are almost eliminated when we properly choose the normalized velocity and static pressure.

## 6. FURTHER APPLICATIONS OF THE PRESENT METHOD

For a three-dimensional ship model in a wind tunnel, this numerical procedure can be used to search for a sector of the stern region where the velocity and static pressure are nearly uniform over the sector. The computed velocity and static pressure at the same point with and without the wind tunnel walls are selected as reference parameters. The distribution of static pressure coefficients around the ship hull in a wind tunnel, normalized by the selected reference velocity and static pressure, can then be considered to be the same as in free flight. However, the three-dimensional boundary-layer displacement effect on the model must be included in the numerical simulation.

If the tunnel blockage is larger than 10%, flow liners inside the tunnel may be used to reduce the wall effect, especially in the regions of the ship bow and stern. The same computation method presented in this paper can be used to design the flow liners needed to simulate the free-flight condition. An off-body surface, at least one boundary-layer thickness away from the hull surface, must be selected to compare the computed distributions of static pressure coefficients with and without tunnel walls and flow liners. The liners may be designed to provide the same distributions of static pressure coefficients, which are normalized by the reference velocity and static pressure at the same selected point, as without the presence of the tunnel walls and liners.

## 7. CONCLUSION

The experimental measurements of velocity and pressure distributions around an axisymmetric body inside a large wind tunnel and the simple numerical simulations of flow with and without the tunnel walls are presented in this paper to demonstrate the physics of tunnel wall effects. A simple potential-flow panel code with viscous-flow correction has been used to locate a transverse reference plane where the computed velocities and local pressures are almost uniform. This plane can be located numerically. Then experimentally, a pitot tube is positioned at the reference plane to measure the reference velocity and static pressure. When measured or computed velocity and static pressure coefficients normalized by the measured or computed reference velocity and static pressure, the entire flow field inside the wind tunnel is found to be very similar to that without the presence of tunnel walls. When the blockage ratio is moderate (e.g. <10%), the tunnel blockage effect is almost completely removed by this presentation of experimental data. This numerical method is proposed to be extended and treat the general three-dimensional ship hull and to design flow liners when the blockage ratio is larger than 10%.

## REFERENCES

1. Liu, H.L., Jiang, C.W., Fry, D.J. and Chang, M.S., "Installation and Pre-test Analysis of Darpa Suboff Model in the DTRC Anechoic Wind Tunnel," DTRC/SHD-1298-04, March 1990.

2. Maskew, B. "Prediction of Subsonic Aerodynamic Characteristics - A Case for Low-Order Panel Methods," AIAA 19th Aerospace Sciences Meeting, Paper 81-0252, St. Louis, Missouri, January 1981.

3. Cebeci, T. and A.M.O. Smith, *Analysis of Turbulent Boundary Layer*, Academic Press, New York, 1974.

4. Wang, H.T. and T. T. Huang, "Calculation of Potential Flow/Boundary Layer Interaction on Axisymmetric Bodies," ASME Symposium on Turbulent Boundary Layers, Niagara Falls, New York. pp. 47-57, 18-20 June 1979.

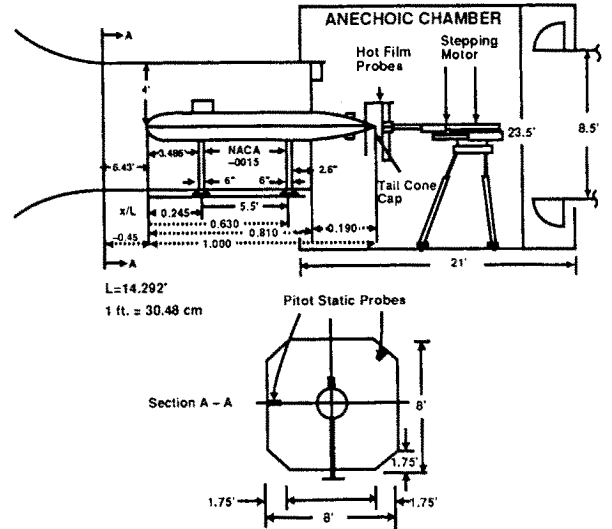


Figure 2 - Schematic View of Model in Closed and Open-Jet Test Section

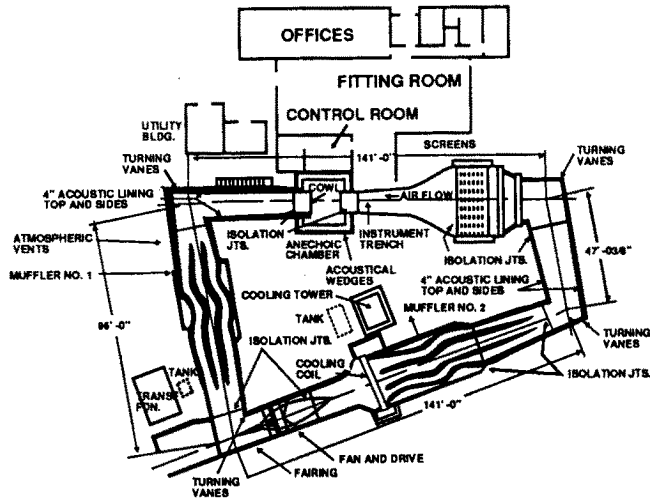


Figure 1 - Schematic of AFF

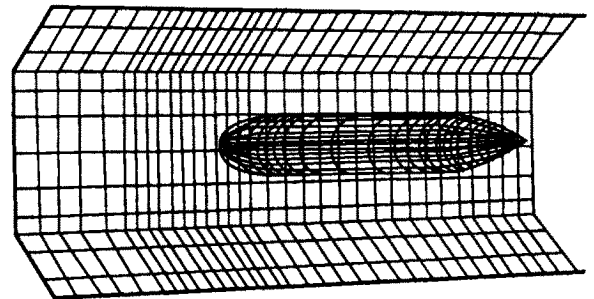


Figure 3 - Grid Representation of Axisymmetric Hull of DTRC Model 5471

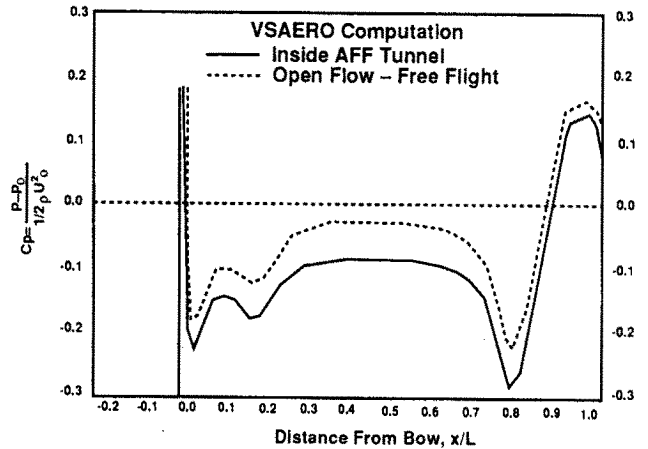


Figure 4 - Effect of Tunnel Blockage on the Computed Surface Pressure Coefficients

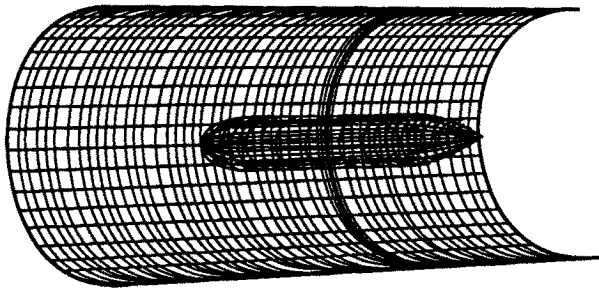


Figure 5 - Grid Representation of Axisymmetric Hull in a Circular Tunnel

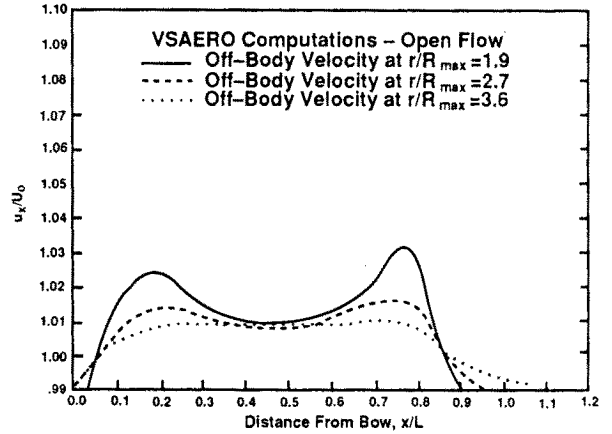


Figure 7b - Computed Off-Body Velocities - Open Flow

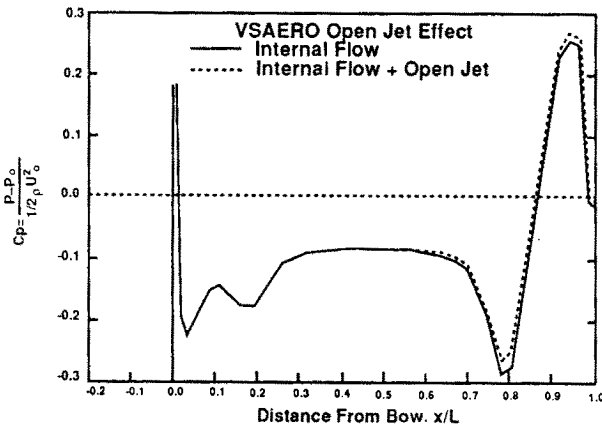


Figure 6 - Effect of a Jet Region on Computed Surface Pressure Coefficients

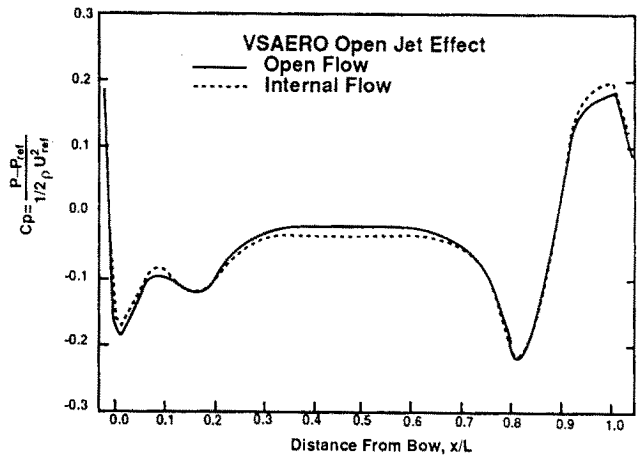


Figure 8 - Effect of the Tunnel Blockage on the Computed Surface Pressure Coefficients of a Displacement Model 5471 Normalized With  $U_{ref}$  at  $x/L=0.85$

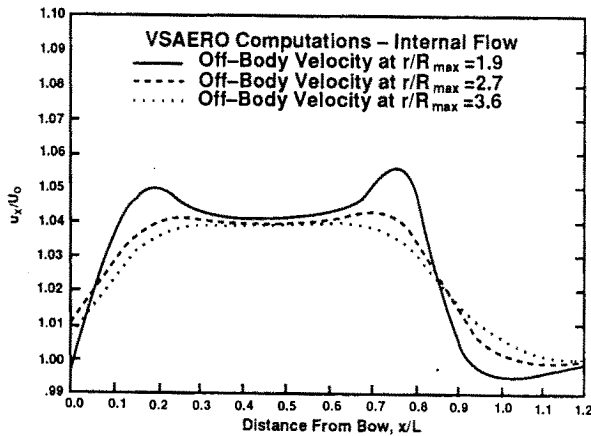


Figure 7a - Computed Off-Body Velocities Inside the Tunnel - Internal Flow

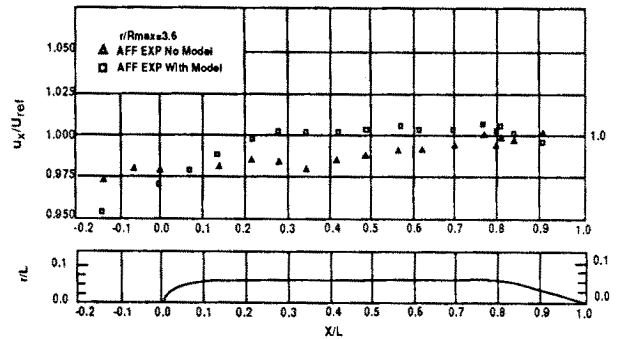


Figure 9 - Measured Tunnel Velocity Variation Along the Ceiling With/Without Model Normalized With  $U_{ref}$  at  $X/L=0.85$

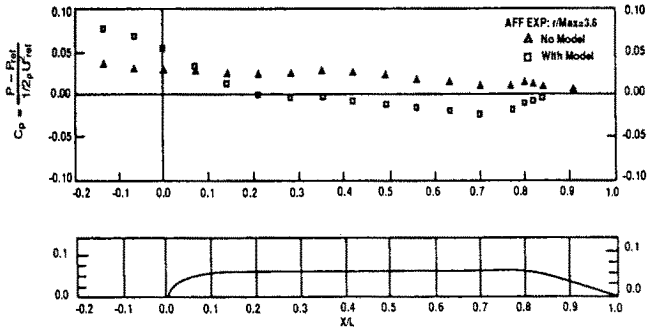


Figure 10 - Measured Tunnel Static Pressure Variation Along the Ceiling With/Without Model Normalized With  $U_{ref}$  and  $P_{ref}$  at  $X/L=0.85$

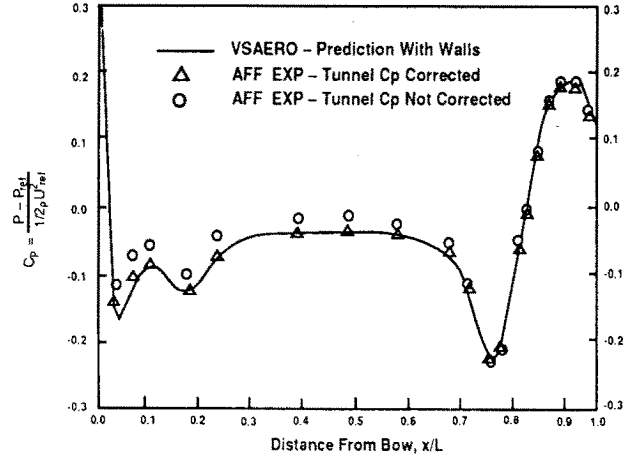


Figure 13 - Comparison of Static Pressure Distributions Prediction Versus Measurements With Tunnel Wall Effect and Longitudinal Pressure Gradient Corrections

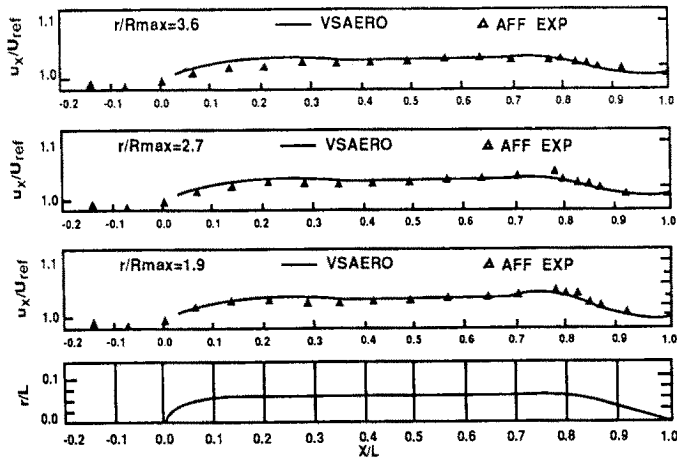


Figure 11 - Comparison Of Measured and Computed Velocities Along the Tunnel Axis Normalized With  $U_{ref}$  at  $x/L=0.85$

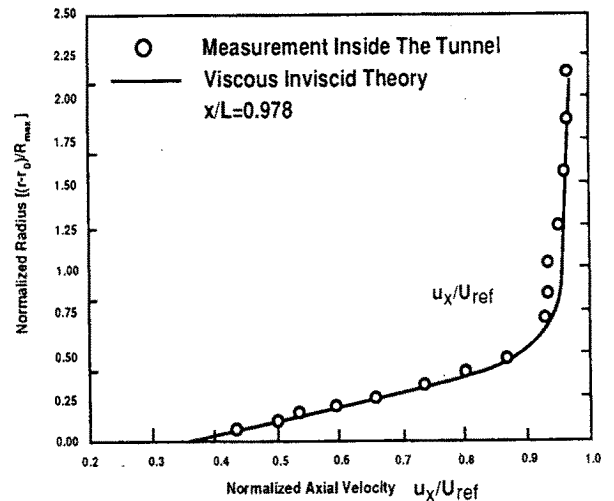
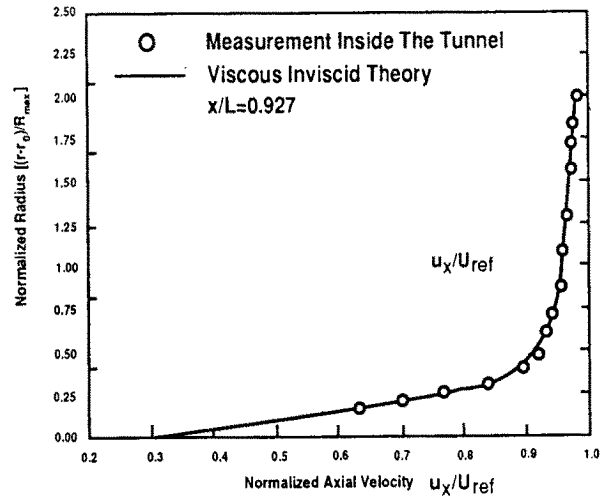


Figure 14 - Comparison of Stern Velocity Profiles Measured Inside the Tunnel and Computed With and Without Tunnel Wall Effect Corrections

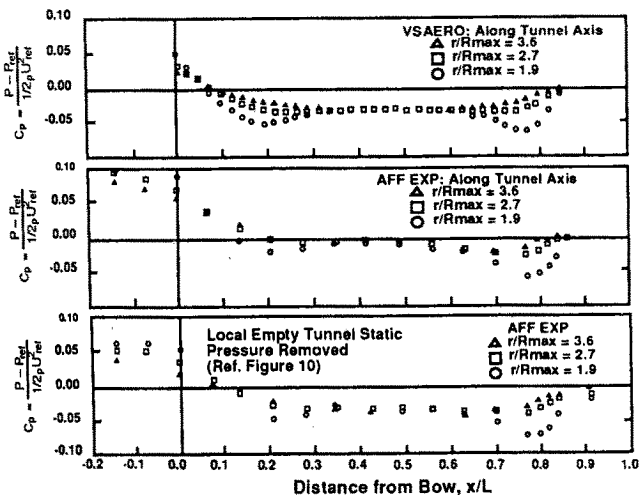


Figure 12 - Tunnel Static Pressure Computations and Measurements Along the Ceiling Centerline